Published in final edited form as:

Lab Chip. 2020 September 21; 20(18): 3399–3409. doi:10.1039/d0lc00378f.

Acoustofluidic multi-well plates for enrichment of micro/nano particles and cells

Pengzhan Liu[a,b], **Zhenhua Tian**[c], **Nanjing Hao**[a], **Hunter Bachman**[a], **Peiran Zhang**[a], **Junhui Hu**[b], **Tony Jun Huang**[a]

[a]Department of Mechanical Engineering and Materials Science, Duke University, Durham, NC 27708, USA.

[b]State Key Lab of Mechanics and Control of Mechanical Structures, Nanjing University of Aeronautics and Astronautics, Nanjing 210016, China.

[c]Department of Aerospace Engineering, Mississippi State University, Starkville, MS 39762, USA.

Abstract

Controllable enrichment of micro/nanoscale objects plays a significant role in many biomedical and biochemical applications, such as increasing the detection sensitivity of assays, or improving the structures of bio-engineered tissues. However, few techniques can perform concentrations of micro/nano objects in multi-well plates, a very common laboratory vessel. In this work, we develop an acoustofluidic multi-well plate, which adopts an array of simple, low-cost and commercially available ring-shaped piezoelectric transducers for rapid and robust enrichment of micro/nanoscale particles/cells in each well of the plate. The enrichment mechanism is validated and characterized through both numerical simulations and experiments. We observe that the ring-shaped piezoelectric transducer can generate circular standing flexural waves in the substrate of each well, and that the vibrations can induce acoustic streaming near the interface between the substrate and a fluid droplet placed within the well; this streaming can drive micro/nanoscale objects to the center of the droplet for enrichment. Moreover, the acoustofluidic multi-well plate can realize simultaneous and consistent enrichment of biological cells in each well of the plate. With merits such as simplicity, controllability, low cost, and excellent compatibility with other downstream analysis tools, the developed acoustofluidic multi-well plate could be a versatile tool for many applications such as micro/nano fabrication, self-assembly, biomedical/biochemical sensing, and tissue engineering.

tony.huang@duke.edu, ejhhu@nuaa.edu.cn.

Author contributions

P.L. and Z.T. planned and designed the research; P.L. performed the simulation; P.L. and N.H. performed the experiments; P.L. fabricated the device; P.L. and P.Z. prepared the cells. P.L., Z.T., J.H. and T.J.H. conceived the idea; P.L., Z.T. and H.B. wrote the draft, and all authors contributed to editing the manuscript.

††Electronic Supplementary Information (ESI) available. See DOI: https://doi.org/10.1039/d0lc00378f

Conflicts of interest

T.J.H. has co-founded a start-up company, Ascent Bio-Nano Technologies Inc., to commercialize technologies involving acoustofluidics and acoustic tweezers.

Introduction

Controllable enrichment of micro/nanoscale objects has considerable applications in various fields, such as micro/nano assembly,[1-4] micro/nano fabrication,[5-7] biomedical/biochemical dection,[8-12] tissue engineering,[13-15] and so forth. As a result, researchers have developed many sample enrichment methods based on various principles, such as optical,[16, 17] dielectrophoretic (DEP),[18, 19] magnetic,[20, 21] mechanical,[22] hydrodynamic,[23] and acoustic methods.[8-10, 24-28] Among them, acoustic-based enrichment methods generally have several advantages, such as high biocompatibility,[8] versatility,[9, 29] simplicity,[30] and fast and efficient actuation.[31, 32] Typically, acoustic-based micro/nano concentration methods rely on two types of mechanisms, i.e., the acoustic radiation force[33-38] or the drag force induced by the acoustic streaming.[39-43] When the sizes of manipulated objects are in the micrometer to millimeter range, the acoustic radiation force is normally dominant and allows for trapping and concentration of objects effectively.[44-49] However, if the scale of the manipulated objects falls in the nanometer range, it becomes difficult to trap and concentrate the objects when only using the acoustic radiation force; this is because the acoustic radiation force is proportional to the object's volume.[33] In these cases, acoustic streaming,[39, 40, 50] which is defined as the second-order steady flow induced by the first-order acoustic field in a fluid, has proven to be an effective mechanism for trapping and concentrating both microscale and nanoscale objects.[9, 51-53]

Although significant efforts have been devoted to developing these acoustic-based enrichment methods and tools,[54] they have seen limited use in practical applications. One could hypothesize that this lack of adoption is due to an inherent resistance to changing established biological protocols; that is, many researchers are hesitant to adopt novel technologies that may alter the time-tested research pathway. For example, even though numerous microfluidic technologies for cell culture have been created,[8, 45] researchers still primarily rely on multi-well plates for conducting large-scale biological investigations.[55] The multi-well plate has seen little change over the last several decades, with many technologies being developed to fit the platform, as opposed to making a new platform altogether. For that reason, figuring out a way to integrate acoustofluidic manipulation technologies into tried and true biological systems is the most direct way to bring the benefits of this method to a broader audience.

In the past years, researchers have already made efforts to integrate acoustofluidic technologies with multi-well plates, and several functions have been demonstrated, including microparticle/cell concentration,[56-58] fluid mixing,[59] and droplet jetting/ejection.[59] However, there is still significant room for improvement in terms of functionalities, versatility, efficiency, and robustness. For example, in these platforms only particles larger than 10 μm have been manipulated and sub-micro particle manipulation has not been demonstrated.

In this work, we develop an acoustofluidic multi-well plate comprised of an array of piezoelectric rings for fast and robust enrichment of micro/nanoscale particles/cells in each well of the plate. Through both computational explorations and experimental demonstrations, we find that the enrichment of micro/nanoscale objects within a droplet

placed at the center of a single well is accomplished on the basis of the inward radial acoustic streaming near the droplet-substrate interface, which is induced by circular standing flexural waves in the substrate of each well. Moreover, the acoustofluidic multi-well plates can consistently realize simultaneous enrichment of biological cells in each well of the plates. With advantages such as simplicity, controllability, low cost, low power consumption, and most importantly, compatibility with existing commercial or standard platforms, our developed acoustofluidic multi-well plate could be a powerful tool for numerous applications in biology, chemistry and medicine.

Materials and methods

Device design and working principle

Figures 1(a) and 1(b) provide a schematic and a photo of the acoustofluidic multi-wall plate, respectively. As shown in these figures, a piezoelectric ring (wire leads soldered on one side) is manually bonded onto the glass bottom of each well of the Glass Bottom 6-well plate (P06G-0-20-F, MatTek Co., USA) using an epoxy layer (Permatex, USA). Although it is difficult to precisely control the thickness of the epoxy layer, we tried to make the epoxy layer as thin and uniform as possible to ensure the vibration transmission efficiency from piezoelectric rings to glass slides. The bandwidth of working frequency of the manually fabricated device prototype is about 3 kHz. The piezoelectric ring (SMR1357T12R412WL, STEINER & MARTINS, Inc., USA), which is aligned to be concentric with the glass bottom, has an inner diameter of 7 mm, an outer diameter of 13.5 mm, and a thickness of 1.2 mm. The detailed material properties of the piezoelectric ring are given in the Supplementary Information.

To investigate the enrichment performance of the proposed device, we focus on one unit (a single well) of the acoustofluidic multi-well plate (Figure 1(c)). Figure 1(d) provides a schematic to illustrate the working principle of the enrichment process for micro/nanoscale objects within a well. When a sinusoidal voltage excitation signal at the unit’s resonance frequency is applied to the piezoelectric ring, circular standing flexural waves that are centrally symmetric with respect to the glass slide’s center, are generated in the glass slide, and the wave energy can then be transmitted into Circular standing flexural waves the suspension droplet at the center of the glass slide. Subsequently, inward radial acoustic streaming is generated near the droplet-substrate interface and is utilized to concentrate micro/nanoscale objects to the center of the well’s glass slide. The working mechanism of our device is further investigated and characterized in the Simulation Results subsection.

Experimental setup

The experiments were conducted on the stage of an inverted microscope (Nikon TE2000U, Japan). The excitation signals for the piezoelectric rings were generated by a function generator (SDG1050, SIGLENT, Germany). Images and videos were taken using Nikon imaging software (NIS-Advanced, Nikon, Japan) through a CCD (charge coupled device) digital camera (CoolSNAP HQ2, Photometrics, Tucson, AZ, USA). The fluorescence intensities in the images were post-analyzed with ImageJ (NIH, USA) software.

Particle and cell sample preparation

8, 15, and 30 μm fluorescent green polystyrene beads (Phosphorex, Inc., USA) were chosen as the microscale particles of interest and the 470 nm fluorescent nile red carboxyl magnetic particles (Spherotech, Inc., USA) were chosen as the nanoscale object used during our investigations. The particles were mixed in deionized (DI) water and ultrasonically treated for 1 min to form particle suspensions. Unless otherwise specified, the approximate concentrations of 8 μm, 15 μm, 30 μm, and 470 nm particles used in the experiments are 0.10 mg/mL, 0.20 mg/mL, 0.20 mg/mL, and 0.10 mg/mL, respectively.

Two types of cell samples, MCF7 and Hela cells were cultured in Dulbecco's Modified Eagle Medium (DMEM, Gibco, Life Technologies, MA, USA) containing 10% fetal bovine serum (Gibco, Life Technologies, MA, USA) and penicillin streptomycin (Gibco, Life Technologies, MA, USA), respectively. All the cells were maintained in 5% CO_2, 37 °C cell culture incubators (HERACELL VIOS 160i CO_2 Incubator, Thermo Scientific, USA). Cell suspensions for all the experiments were made by dissociation of cells with trypsin-EDTA (Gibco, Life Technologies, NY, USA), centrifugation of dissociated cells at 800 rpm for 5 min at room temperature, and re-suspension in the growth media. Cell densities were estimated using a hemocytometer (HAUSSER SCIENTIFIC, USA). Living cells were labelled with green fluorescence using Calcein-AM (Invitrogen, Life Technologies, MA, USA).

2D axisymmetric model for the finite element simulations

To investigate the enrichment mechanism of our acoustofluidic multi-well plate, we simplified one unit of the device (Figure 1(c)) to a 2D axisymmetric physical model (Figure S1). We simulated the flexural waves in the glass slide as well as the acoustic pressure field and acoustic streaming field in the droplet. The commercial finite element analysis (FEA) software COMSOL Multiphysics 5.5 (Burlington, MA, USA) was utilized for the numerical simulations.

In the first step of the simulation, the resonance frequency of the system was computed using the Thermoviscous Acoustic-Piezoelectric-Solid Interaction module and the Eigenfrequency solver. In the second step, the simulated resonance frequency (109.2 kHz), which was found to be close to the frequency (112 kHz) used for enrichment during experimentation, was selected to simulate flexural waves in the glass slide and the acoustic field in the droplet using the Frequency Domain solver. The difference between the simulated and experimental resonance frequencies may result from inherent inconsistencies introduced during the fabrication and assembly of the prototype device.[30,60] In the third step, with the computational results for the acoustic field, the steady acoustic streaming field in the droplet is simulated using the Laminar Flow module based on the Reynolds stress method and a Stationary solver.[29,39,61-64]

Unless otherwise specified, the material parameters used in the numerical simulations are listed in Table SI. As shown in Figure S1, the droplet volume used in the simulation model is 15 μL, and the corresponding radius and height of the droplet are 3.2 mm and 0.9 mm, respectively. According to the experimental measurement result, the thickness of the epoxy

layer is set to be 0.2 mm. The boundary conditions for simulations of acoustic field and acoustic streaming field are shown in Figures S2 and S3, respectively, and the mesh plot of the whole 2D axisymmetric model is shown in Figure S4. In the solid domain, the element numbers in the glass slide, epoxy layer, and piezoelectric ring are 217924, 248, and 1261, respectively. In the fluid domain (droplet), the computational mesh is generated from a maximum element size 0.3δ at the fluid domain boundaries and a maximum element size in the bulk of the fluid domain given by 10δ, where δ (1.71 μm) is the thickness of viscous boundary layer in water at 109.2 kHz,[65] and the resultant total element number is 461822. The mesh convergence and independence for simulating acoustofluidic fields in the fluid domain have been tested and verified by many investigations.[65-68]

Results

Simulation results

Based on the above described simulation scheme, we performed the numerical simulations for the 2D axisymmetric acoustofluidic model. Figure 2(a) shows the simulated displacement field with circular standing flexural waves of one acoustofluidic element which is excited by a 109.2 kHz and 6 V_{pp} signal. Circular standing flexural waves can be seen in the glass slide, and these circular standing flexural waves are generated by the radial extension vibration mode of the piezoelectric ring (Figure S5). For quantitative characterization, the simulated wave displacement amplitudes along the radial direction (r) under different driving voltages are compared in Figure 2(b). It is seen that the wave displacement amplitude is maximized at the center of the glass slide and grows with an increase in the driving voltage. Figure 2(c) shows the simulated acoustic pressure amplitude distribution in the droplet, from which it can be seen that the acoustic pressure amplitude at the central position is maximum. In this regard, one may expect that particles/cells with positive acoustic contrast factors will never aggregate in the region of high acoustic pressure because the acoustic radiation force will repel these objects from the region of high acoustic pressure to that of low acoustic pressure.[33, 69] However, from the simulated acoustic streaming field in the droplet shown in Figure 2(d), it is seen that near the droplet-substrate interface, as the acoustic streaming flows towards the central area in the $0 < r < 1.3$ mm region, micro/nanoscale objects can be driven to the central area and be concentrated there. Based on our simulation, the streaming velocity outside of this region varies in direction, not always pointing towards the center and yielding aggregation. Thus, we consider the $0 < r < 1.3$ mm region as the concentration zone. Through simulation results, we also found that the order of magnitude of the acoustic radiation force is negligible compared to that of the drag force induced by acoustic streaming near the droplet-substrate interface. Therefore, we can verify that the acoustic streaming is dominant in our device and the enrichment of micro/nanoscale objects is achieved based on the acoustic streaming that occurs near the droplet-substrate interface.

To quantitatively characterize the dependency of the acoustic streaming field on the experimental conditions, as shown in the acoustic streaming's profile in the viscous boundary layer (Figure S6), we extracted the tangential acoustic streaming velocity value u_r at the outside boundary of the viscous boundary layer in the $0 < r < 1.3$ mm region. Figure

2(e) shows the simulated tangential acoustic streaming velocity distribution at the outside boundary of the viscous boundary layer under different driving voltages, from which it is seen that u_r increases from zero at the center of the droplet to its maximum value at approximately r = 0.6 mm, and then descends with a further increase of r. For the convenience of characterization, we extract the maximum value of acoustic streaming velocity in Figure 2(e) as u_{max} and also define the mean value of tangential acoustic streaming velocity u_{mean} as

$$u_{mean} = \frac{\int_0^{1.3\,mm} u_r dr}{1.3\,mm} \quad (1)$$

The relationship between u_{max}, u_{mean}, and driving voltage is shown in Figure 2(f), and it can be seen that as the driving voltage rises, both u_{max} and u_{mean} increase. Moreover, we simulated the tangential acoustic streaming velocity distribution at the outside boundary of the viscous boundary layer in the $0 < r < 1.3$ mm region under different droplet volumes, and the result is shown in Figure 2(g). Figure 2(h) shows the relationship between u_{max}, u_{mean}, and droplet volume, from which it is seen that when the droplet volume increases from 5 μL to 15 μL, both u_{max} and u_{mean} increase. This is because when the droplet volume increases properly, more acoustic energy can be transmitted into the droplet, which can result in stronger acoustic streaming velocity within the droplet. However, when the droplet volume is 20 μL, both u_{max} and u_{mean} decrease compared to those when the droplet volume is 15 μL. This phenomenon may be attributed to the fact that when the droplet volume is too large, the heavy acoustic load resulting from the large droplet on the device may affect and weaken the device's vibration to a certain extent,[30, 60] which thus causes a weaker acoustic field in the droplet and a correspondingly weaker acoustic streaming velocity near the droplet-substrate interface.

Enrichment of 8 and 15 μm fluorescent polystyrene particles

Figure 3(a) shows the concentration process of 8 μm fluorescent polystyrene particles within a single unit of the acoustofluidic multi-well plate when the driving voltage, frequency, droplet volume, and particle concentration are 6 V_{pp}, 112 kHz, 15 μL, and 0.10 mg/mL, respectively (Movie S1). The initial distribution of 8 μm fluorescent polystyrene particles on the substrate in the panorama of the microscope is shown in Figure S7. It can be seen in Figure 3(a) that 8 μm polystyrene particles can gradually aggregate in the central area at the droplet-substrate interface with an increase in acoustic field time, which results in a gradual increase in fluorescence intensity in the central area as well. Figure 3(b) shows the enrichment process of 15 μm fluorescent polystyrene particles with a single unit of the acoustofluidic multi-well plate when the driving voltage, frequency, droplet volume, and particle concentration are 6 V_{pp}, 112 khlz, 15 μL, and 0.20 mg/mL, respectively (Movie S2). The initial distribution of 15 μm fluorescent PS particles on the substrate in the panorama of the microscope is shown in Figure S8. It is seen from Figure 3(b) that in the initial 10 s, 15 μm polystyrene particles can rapidly aggregate in the central area at the droplet-substrate interface, after which the particle aggregation process equilibrates and the cluster maintains

its size, which indicates that all of the particles within the effective acoustic streaming field have been concentrated.

For 15 μm fluorescent polystyrene particles, the experimentally measured average fluorescence intensities in the central area versus acoustic field time under different driving voltages are compared in Figure 3(c); the droplet volume and particle concentration are 15 μL and 0.20 mg/mL, respectively. Comparable results for 8 μm fluorescent polystyrene particles are shown in Figure S9. It can be seen that the fluorescence intensity rapidly increases in the first 10 s of acoustic field and then remains constant, which indicates that all the particles within the effective zone of acoustic streaming have been concentrated in the central area at the droplet-substrate interface. Also, as predicted by the faster acoustic streaming velocity near the droplet-substrate interface when applying a larger driving voltage (Figure 2(f)), the fluorescence intensity increases as the driving voltage increases. The fluorescence intensities versus acoustic field time under different droplet volumes for 15 μm fluorescent polystyrene particles are compared in Figure 3(d) when the driving voltage and particle concentration are 6 V_{pp} and 0.20 mg/mL, respectively, and the result for 8 μm fluorescent polystyrene particles is shown in Figure S10. It is seen that the fluorescence intensity in the 15 μL droplet grows fastest and reaches its equilibrium value first, which is consistent with the simulations that predicted the greatest acoustic streaming velocity near the droplet-substrate interface for a 15 μL droplet (Figure 2(h)); this result was also verified experimentally by measuring the velocity of individual 15 μm polystyrene particles in suspension droplets of varying size (Figure S11). After 30 s, the fluorescence intensity in the 20 μL droplet surpasses that in the 15 μL droplet, which results from more fluorescent polystyrene particles being available for concentration at the droplet-substrate interface in the 20 μL droplet. The fluorescence intensities versus acoustic field time under different particle concentrations for 15 μm and 8 μm fluorescent polystyrene particles are compared in Figures S12 and S13 when the driving voltage and droplet volume are 6 V_{pp} and 15 μL, respectively. Furthermore, we experimentally measured the relationship between the stable fluorescence intensity after acoustic field and particle concentration when the diving voltage and droplet volume are maintained at 6 V_{pp} and 15 μL, respectively; the result is shown in Figure 3(e). It is seen that the stable fluorescence intensity follows a linear trend with regards to the variation of particle concentration, which indicates that our device could be used as a quantitative assay for particle concentration.

Fluorescent signal enhancement for 30 μm and 470 nm particles

Having demonstrated the enrichment performance of a single unit of our acoustofluidic multi-well plate in detail, we further experimentally characterize the fluorescent signal enhancement capability accomplished by a single unit of our device for larger and smaller fluorescent particles, i.e., 30 μm polystyrene particles and 470 nm carboxyl magnetic particles. We chose 470 nm carboxyl magnetic particles over polystyrene nanoparticles of a similar size for this demonstration because we experimentally observed that although the inward radial acoustic streaming near the droplet-substrate interface could drag polystyrene nanoparticles to the central area, the upward acoustic streaming (Figure 2(d)) would lift polystyrene nanoparticles up from the substrate, meaning that polystyrene nanoparticles could not be stably concentrated; however, the heavier magnetic nanoparticles were able to

be concentrated at the bottom of the fluid domain along the droplet-substrate interface similar to larger polystyrene particles. The detailed force analysis of a still single particle at the center of the droplet-substrate interface in the acoustofluidic field, as well as a discussion of the relationship between particle size, density, and enrichment potential, are given in the Supplementary Information.

Figure 4(a) shows the initial random distribution of 30 μm polystyrene particles in the central area at the droplet-substrate interface when the droplet volume and particle concentration are 15 μL and 0.20 mg/mL, respectively. Figure 4(b) shows the aggregation of 30 μm polystyrene particles after 10 s of acoustic field with a 6 V_{pp} driving voltage and 112 kHz excitation frequency. Furthermore, we experimentally measured the fluorescent signal enhancement ratio between particle concentration results obtained before and after 10 s of acoustic field, and the fluorescent signal enhancement ratio versus driving voltage is shown in Figure 4(c); the signal enhancement ratio is defined as the ratio between the mean fluorescence intensity of an image without acoustic field and the mean fluorescence intensity of a photo with 10 s of acoustic field. It is seen that when the driving voltage increases from 4 V_{pp} to 10 V_{pp}, the signal enhancement ratio can increase from 4.5 to 7. Figure 4(d) shows the initial random distribution of 470 nm carboxyl magnetic particles in the central area at the droplet-substrate interface when the droplet volume and particle concentration are 15 μL and 0.10 mg/mL, respectively. Figure 4(e) shows the aggregation of 470 nm carboxyl magnetic particles after 1 min of acoustic field with an 8 V_{pp} driving voltage and 112 kHz excitation frequency. Also, we experimentally measured the fluorescent signal enhancement ratio between particle concentration results obtained before and after 1 min of acoustic field, and the fluorescent signal enhancement ratio versus driving voltage is shown in Figure 4(f). It is seen that when the driving voltage changes from 4 V_{pp} to 6 V_{pp}, the signal enhancement ratio increases insignificantly, which indicates that the engendered acoustic streaming velocity is not large enough to concentrate the nanoparticles. However, when the driving voltage increases from 6 V_{pp} to 10 V_{pp}, the fluorescent signal enhancement ratio increased from 1.6 to 3 with a relatively large acoustic streaming velocity near the droplet-substrate interface.

Enrichment of cells in the acoustofluidic multi-well plates

To demonstrate the enrichment capability of our acoustofluidic multi-well plate for biological samples, we first perform the simultaneous enrichment of cells in each well of the acoustofluidic 6-well plate (Figure 1(b)). Before the experiments, we pre-coated all the wells with a 0.5% Bovine Serum Albumin (BSA, Sigma-Aldrich, Co., USA) phosphate buffered saline (PBS, Gibco, Life Technologies, NY, USA) solution for 24 h to reduce the adhesion between cells and the glass bottom. In the experiments, we input the AC signal to the 6 piezoelectric rings simultaneously from the same channel. Figure 5(a) shows the stained MCF7 cell aggregations in wells 1-6 after 2 min of acoustic field when the driving voltage, frequency, droplet volume, and cell concentration are 10 V_{pp}, 110 kHz, 10 μL, and 10^6 cells/mL, respectively. Furthermore, we experimentally measured and compared the fluorescence intensities of stained MCF7 cell aggregations in wells 1-6 after 2 min of acoustic field under different cell concentrations, and the result is shown in Figure 5(b). From Figure 5(b), we calculated that the maximum deviation of fluorescence intensity is no

more than 15%. Since the integrated device was fabricated manually, the performance consistency for each well of the prototype can be further improved with more standardized fabrication technologies.

We also fabricated an acoustofluidic 12-well plate integrated with an array of 12 piezoelectric rings, and the prototype is shown in Figure 5(c). Before the experiments, we also pre-coated all the wells with a 0.5% BSA PBS solution for 24 h. In the experiments, we applied an AC signal to the 12 piezoelectric rings simultaneously from the same channel. Figure. 5(d) shows the stained Hela cell aggregations in wells 1-12 after 2 min of acoustic field when the driving voltage, frequency, droplet volume, and cell concentration are 10 V_{pp}, 109 kHz, 10 μL, and 1.6×10^6 cells/mL, respectively. Moreover, we experimentally measured and compared the fluorescence intensities of stained Hela cell aggregations in wells 1-12 after 2 min of acoustic field under different cell concentrations, and the result is shown in Figure 5(e). From Figure 5(e), we calculated that the maximum deviation of fluorescence intensity was as low as 6%, which indicates the relative consistency of the prototype device.

To verify the biocompatibility of our device, we measured the cell viabilities for MCF7 and Hela cells in a single well of the acoustofluidic multi-well plate under two conditions: without acoustic field (control) and with acoustic field (the driving voltage is 10 V_{pp} and the duration for the acoustic field is 2 min). Cell viabilities were estimated by counting the number of live cells stained with Calcein-AM and the total cell numbers in the bright field. Figure 5(f) shows the measurement results of cell viability tests, from which it is seen that the cell viability decreases insignificantly (no more than 3.5%) after the device is in the acoustic field for 2 min. Therefore, it can be generally concluded that the acoustic streaming induced in the cell suspension droplet has minimum damage to cells.

Conclusions and Discussion

In this article, we have developed and demonstrated an acoustofluidic multi-well plate which enables rapid and robust enrichment of micro/nanoscale objects within suspension droplets placed at the center of a single well. The mechanism of enrichment is based on the inward radial acoustic streaming near the droplet-substrate interface, which is caused by the circular standing flexural waves of the glass substrate. The experimental results have confirmed that the acoustofluidic multi-well plate can be very effective for micro/nano enrichment when the scale of manipulated objects ranges from 400 nm to 30 μm. During our investigation, we showed that our platform could be used to measure particle sample concentrations based on a standardized fluorescence intensity versus concentration curve. We also demonstrated the simultaneous enrichment of biological cells in multiple wells.

There is still significant room for improvement when attempting to adapt the technology for use in biological/chemical/biomedical laboratories. Namely, the device has been demonstrated on relatively small multi-well plates, whereas biologists traditionally use much larger systems. Additionally, the current practice of permanently bonding the transducers to the wells is inefficient and impractical for use with the relatively disposable nature of the well-plates. While these factors present a shortcoming of the current implementation of our

technology, in preliminary experimentation we found that when substituting the epoxy bonding process with a more temporary gel-based bonding,[70] concentration can still be achieved effectively (Figure S16). Although this concentration was achieved with a lower efficiency and speed, these results suggest that through further modification, our acoustofluidic concentration method could be adapted to be used in a more reusable manner which aligns with the disposable nature of multi-well plates in laboratory settings; that is, by avoiding permanently bonding the transducers to the multi-well plates, we can reuse the transducers across a larger number of biological tests. This will make the device much more readily adoptable by biologist.

Although the current device was demonstrated for use with small droplet volumes, preliminary investigations suggest that scaling up the device will still allow for generation of an acoustic streaming pattern that concentrates particles in the center of the well. This is promising for developing a larger device for use in applications which require larger sample volumes. Additionally, the results of our simulation suggest that given an optimized transducer and well setup we would be able to achieve concentration even when the well is filled to the walls (not just an isolated droplet). When a single well is filled with a thin layer of cell suspension fluid, we are still able to generate acoustic streaming flows near the center of the well (aligned with the center of the PZT ring) for enrichment.

With attributes and merits such as simplicity, controllability, and biocompatibility, the developed acoustofluidic multi-well plate could be a robust tool for acoustic assisted in-plate tissue culture with high consistency. Additionally, the developed acoustofluidic multi-well plate could be applied for acoustic assisted biomedical/biochemical sensing/detection since the sensing/detection sensitivity could be dramatically enhanced through sample enrichment. Our user-friendly device is simple and compact enough to be integrated with other well-developed standard analysis platforms which rely on multi-well plates.

Supplementary Material

Refer to Web version on PubMed Central for supplementary material.

Acknowledgements

We acknowledge support from the National Natural Science Foundation of China (Grant No. 11974183), the National Institutes of Health (R01GM132603, R01GM135486, UG3TR002978, R33CA223908, R01GM127714, and R01HD086325) and United States Army Medical Research Acquisition Activity (W81XWH-18-1-0242). Pengzhan Liu acknowledges the financial support from the China Scholarship Council (CSC).

References

1. Kim H, Kim T, Kim D and Shim W, Nano Lett, 2016, 16, 6472–6479. [PubMed: 27580002]
2. Sazan H, Piperno S, Layani M, Magdassi S and Shpaisman H, J Colloid Interf Sci, 2019, 536, 701–709.
3. Chen P, Luo ZY, Guven S, Tasoglu S, Ganesan AV, Weng A and Demirci U, Adv Mater, 2014, 26, 5936–5941. [PubMed: 24956442]
4. Destgeer G, Hashmi A, Park J, Ahmed H, Afzal M and Sung HJ, Rsc Adv, 2019, 9, 7916–7921.
5. Nichols MK, Kumar RK, Bassindale PG, Tian LF, Barnes AC, Drinkwater BW, Patil AJ and Mann S, Small, 2018, 14, 1800739.

6. Haslam MD and Raeymaekers B, Compos Part B-Eng, 2014, 60, 91–97.
7. Chen YC, Ding XY, Lin SCS, Yang SK, Huang PH, Nama N, Zhao YH, Nawaz AA, Guo F, Wang W, Gu YY, Mallouk TE and Huang TJ, ACS Nano, 2013, 7, 3306–3314. [PubMed: 23540330]
8. Ozcelik A, Rufo J, Guo F, Gu YY, Li P, Lata J and Huang TJ, Nat Methods, 2018, 15, 1021–1028. [PubMed: 30478321]
9. Mao ZM, Li P, Wu MX, Bachman H, Mesyngier N, Guo XS, Liu S, Costanzo F and Huang TJ, ACS Nano, 2017, 11, 603–612. [PubMed: 28068078]
10. Liu WP, Pan ST, Zhang HX, Tang ZF, Liang J, Wang YY, Zhang ML, Hu XD, Pang W and Duan XX, ACS Central Sci, 2018, 4, 899–908.
11. Cui WW, Mu LY, Duan XX, Pang W and Reed MA, Nanoscale, 2019, 11, 14625–14634. [PubMed: 31240289]
12. Li P and Huang TJ, Anal Chem, 2019, 91, 757–767. [PubMed: 30561981]
13. Tait A, Glynne-Jones P, Hill AR, Smart DE, Blume C, Hammarstrom B, Fisher AL, Grossel MC, Swindle EJ, Hill M and Davies DE, Sci Rep-Uk, 2019, 9, 9789.
14. Serpooshan V, Chen P, Wu H, Lee S, Sharma A, Hu DA, Venkatraman S, Ganesan AV, Usta OB, Yarmush M, Yang F, Wu JC, Demirci U and Wu SM, Biomaterials, 2017, 131, 47–57. [PubMed: 28376365]
15. Armstrong JPK, Puetzer JL, Serio A, Guex AG, Kapnisi M, Breant A, Zong Y, Assal V, Skaalure SC, King O, Murty T, Meinert C, Franklin AC, Bassindale PG, Nichols MK, Terracciano CM, Hutmacher DW, Drinkwater BW, Klein TJ, Perriman AW and Stevens MM, Adv Mater, 2018, 30, 1802649.
16. Zhang Y, Lei JJ, Zhang YX, Liu ZH, Zhang JZ, Yang XH, Yang J and Yuan LB, Sci Rep-Uk, 2017, 7, 14378.
17. Armon N, Greenberg E, Layani M, Rosen YS, Magdassi S and Shpaisman H, ACS Appl Mater Inter, 2017, 9, 44214–44221.
18. Han SI, Kim HS and Han A, Biosens Bioelectron, 2017, 97, 41–45. [PubMed: 28554044]
19. Chen YL and Jiang HR, Biomicrofluidics, 2017, 11, 034102. [PubMed: 28503246]
20. Zeng J, Chen C, Vedantam P, Tzeng TR and Xuan XC, Microfluid Nanofluid, 2013, 15, 49–55.
21. Hejazian M and Nguyen NT, Biomicrofluidics, 2016, 10, 044103. [PubMed: 27478527]
22. Zhou PL, Yu HB, Yang WG, Wen YD, Wang ZD, Li WJ and Liu LQ, ACS Appl Mater Inter, 2017, 9, 16715–16724.
23. Friedrich SM, Burke JM, Liu KJ, Ivory CF and Wang T-H, Nat Commun, 2017, 8, 1213. [PubMed: 29089494]
24. Shilton R, Tan MK, Yeo LY and Friend JR, J Appl Phys, 2008, 104, 014910.
25. Bourquin Y, Syed A, Reboud J, Ranford-Cartwright LC, Barrett MP and Cooper JM, Angew Chem Int Edit, 2014, 53, 5587–5590.
26. Destgeer G, Cho H, Ha BH, Jung JH, Park J and Sung HJ, Lab Chip, 2016, 16, 660–667. [PubMed: 26755271]
27. Tang Q, Wang XF and Hu JH, Appl Phys Lett, 2017, 110, 104105.
28. Fu YQ, Luo JK, Nguyen NT, Walton AJ, Flewitt AJ, Zu XT, Li Y, McHale G, Matthews A, Iborra E, Du H and Milne WI, Prog Mater Sci, 2017, 89, 31–91.
29. Qi XM, Tang Q, Liu PZ, Minin IV, Minin OV and Hu JH, Sensor Actuat B-Chem, 2018, 274, 381–392.
30. Hu J, Ultrasonic Micro/Nano Manipulations: Principles and Examples, World Scientific, Singapore, 2014.
31. Connacher W, Zhang NQ, Huang A, Mei JY, Zhang S, Gopesh T and Friend J, Lab Chip, 2018, 18, 1952–1996. [PubMed: 29922774]
32. Friend J and Yeo LY, Rev Mod Phys, 2011, 83, 647–704.
33. Gor'kov LP, Soviet Physics Doklady, 1962, 6, 773–775.
34. Deshmukh S, Brzozka Z, Laurell T and Augustsson P, Lab Chip, 2014, 14, 3394–3400. [PubMed: 25007385]
35. Bruus H, Lab Chip, 2012, 12, 1014–1021. [PubMed: 22349937]

36. Melde K, Choi E, Wu ZG, Palagi S, Qiu T and Fischer P, Adv Mater, 2018, 30, 1704507.
37. Foresti D, Nabavi M, Klingauf M, Ferrari A and Poulikakos D, P Natl Acad Sci USA, 2013, 110, 12549–12554.
38. Wu MX, Ozcelik A, Rufo J, Wang ZY, Fang R and Huang TJ, Microsystems & Nanoengineering, 2019, 5, 32. [PubMed: 31231539]
39. Lighthill J, J Sound Vib, 1978, 61, 391–418.
40. Nyborg WL, J Acoust Soc Am, 1953, 25, 68–75.
41. Zhang SP, Lata J, Chen CY, Mai J, Guo F, Tian ZH, Ren LQ, Mao ZM, Huang PH, Li P, Yang SJ and Huang TJ, Nat Commun, 2018, 9, 2928. [PubMed: 30050088]
42. Nama N, Huang PH, Huang TJ and Costanzo F, Lab Chip, 2014, 14, 2824–2836. [PubMed: 24903475]
43. Ahmed D, Chan CY, Lin S-CS, Muddana HS, Nama N, Benkovic SJ and Huang TJ, Lab Chip, 2013, 13, 328–331. [PubMed: 23254861]
44. Tian ZH, Yang SJ, Huang PH, Wang ZY, Zhang PR, Gu YY, Bachman H, Chen CY, Wu MX, Xie YB and Huang TJ, Sci Adv, 2019, 5, eaau6062. [PubMed: 31172021]
45. Chen KJ, Wu MX, Guo F, Li P, Chan CY, Mao ZM, Li SX, Ren LQ, Zhang R and Huang TJ, Lab Chip, 2016, 16, 2636–2643. [PubMed: 27327102]
46. Wiklund M and Hertz HM, Lab Chip, 2006, 6, 1279–1292. [PubMed: 17102841]
47. Collins DJ, Morahan B, Garcia-Bustos J, Doerig C, Plebanski M and Neild A, Nat Commun, 2015, 6, 8686. [PubMed: 26522429]
48. Foresti D and Poulikakos D, Phys Rev Lett, 2014, 112, 024301. [PubMed: 24484018]
49. Tung KW, Chung PS, Wu C, Man TX, Tiwari S, Wu B, Chou YF, Yang FL and Chiou PY, Lab Chip, 2019, 19, 3714–3725. [PubMed: 31584051]
50. Schmid L, Wixforth A, Weitz DA and Franke T, Microfluid Nanofluid, 2012, 12, 229–235.
51. Li N, Hu JH, Li HQ, Bhuyan S and Zhou YJ, Appl Phys Lett, 2012, 101, 093113.
52. Yang BJ and Hu JH, Sensor Actuat B-Chem, 2014, 193, 472–477.
53. Collins DJ, Ma ZC, Han J and Ai Y, Lab Chip, 2017, 17, 91–103.
54. Xie YL, Bachman H and Huang TJ, Trac-Trend Anal Chem, 2019, 117, 280–290.
55. Freshney RI, Culture of Animal Cells: A Manual of Basic Technique and Specialized Applications, Wiley-Blackwell, New Jersey, 6th edn., 2010.
56. Sudeepthi A, Sen AK and Yeo L, Microfluid Nanofluid, 2019, 23, 76.
57. Kurashina Y, Takemura K and Friend J, Lab Chip, 2017, 17, 876–886. [PubMed: 28184386]
58. Vanherberghen B, Manneberg O, Christakou A, Frisk T, Ohlin M, Hertz HM, Onfelt B and Wiklund M, Lab Chip, 2010, 10, 2727–2732. [PubMed: 20820481]
59. Rezk AR, Ramesan S and Yeo LY, Lab Chip, 2018, 18, 406–411. [PubMed: 29231220]
60. Zhao C, Ultrasonic motors: technologies and applications, Science Press, Beijing, 2011.
61. Tang Q, Liu PZ and Hu JH, Microfluid Nanofluid, 2018, 22, 46.
62. Su SF, Liu PZ, Tang Q and Hu JH, J Appl Phys, 2018, 124, 244902
63. Liu PZ and Hu JH, Rev Sci Instrum, 2017, 88, 105003. [PubMed: 29092512]
64. Alghane M, Chen BX, Fu YQ, Li Y, Luo JK and Walton AJ, J Micromech Microeng, 2011, 21, 015005.
65. Muller PB, Barnkob R, Jensen MJH and Bruus H, Lab Chip, 2012, 12, 4617–4627. [PubMed: 23010952]
66. Nama N, Barnkob R, Mao ZM, Kahler CJ, Costanzo F and Huang TJ, Lab Chip, 2015, 15, 2700–2709. [PubMed: 26001199]
67. Chen CY, Zhang SP, Mao ZM, Nama N, Gu YY, Huang PH, Jing Y, Guo XS, Costanzo F and Huang TJ, Lab Chip, 2018, 18, 3645–3654. [PubMed: 30361727]
68. Mao ZM, Xie YL, Guo F, Ren LQ, Huang PH, Chen YC, Rufo J, Costanzo F and Huang TJ, Lab Chip, 2016, 16, 515–524. [PubMed: 26698361]
69. Gu YY, Chen CY, Wang ZY, Huang PH, Fu H, Wang L, Wu MX, Chen YC, Gao TY, Gong JY, Kwun J, Arepally GM and Huang TJ, Lab Chip, 2019, 19, 394–402. [PubMed: 30631874]

70. Chen Y, Li S, Gu Y, Li P, Ding X, Wang L, McCoy JP, Levine SJ and Huang TJ, Lab Chip, 2014, 14, 924–930. [PubMed: 24413889]

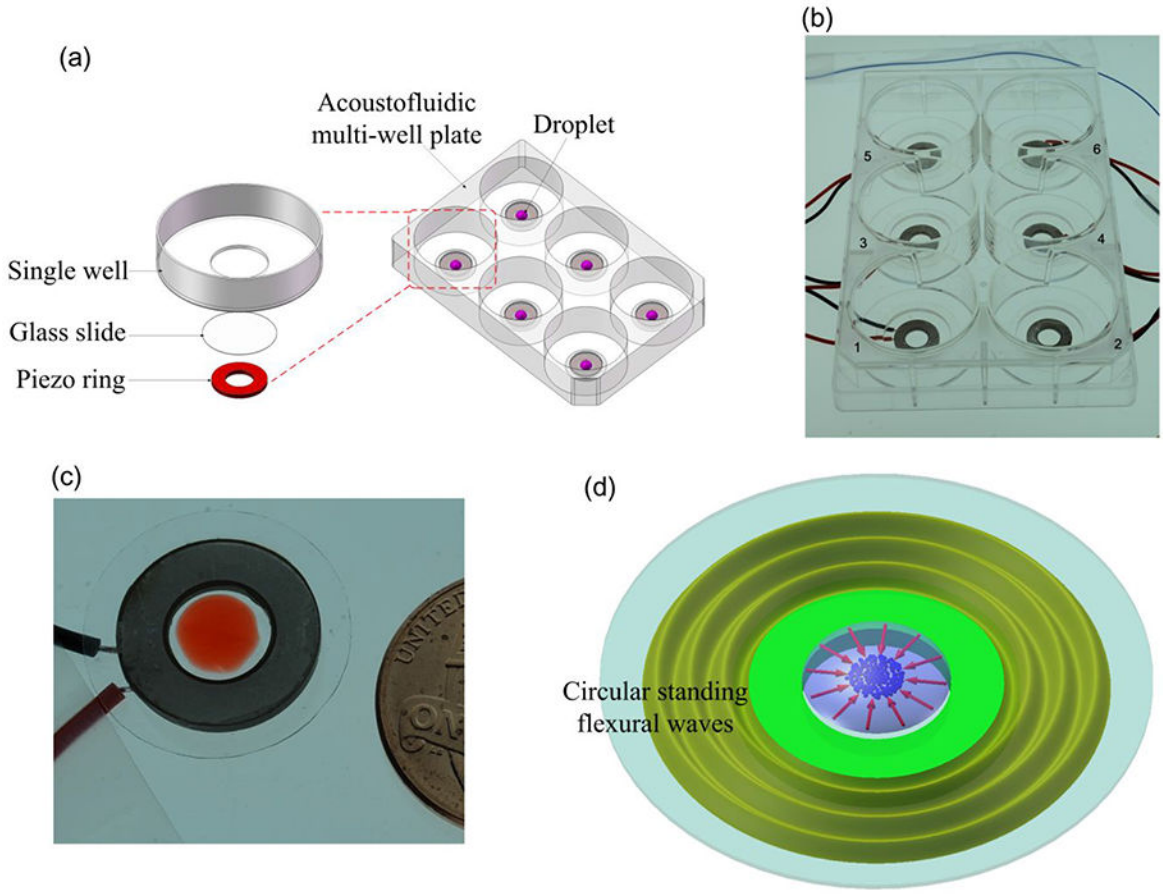

Figure 1.

(a) Schematic of the acoustofluidic multi-well plate. **(b)** Photograph of the fabricated acoustofluidic multi-well plate. **(c)** Photograph of a single unit of the acoustofluidic multi-well plate. **(d)** Schematic of the working principle of enriching micro/nanoscale objects in one unit of the acoustofluidic multi-well plate.

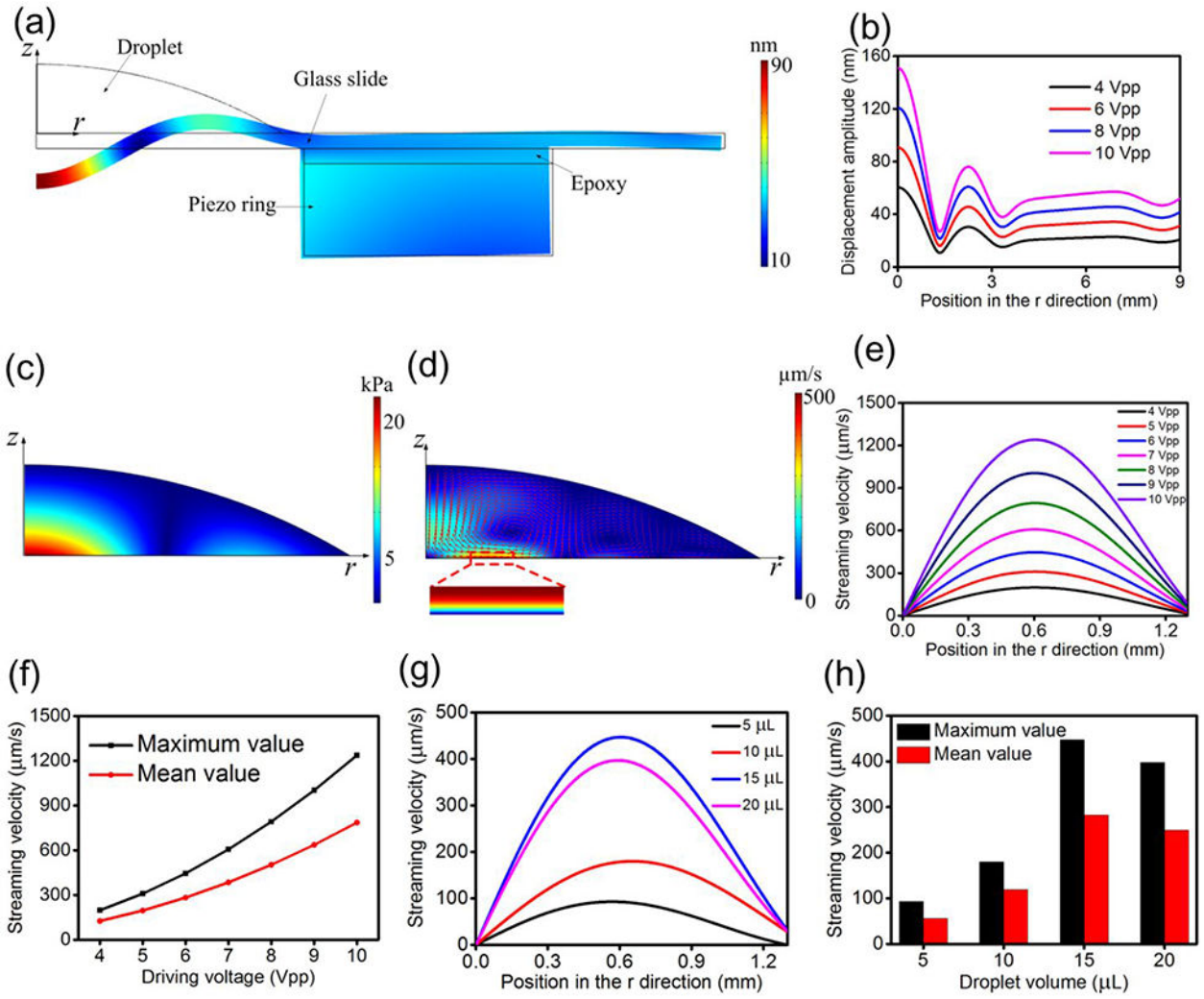

Figure 2.

(a) Simulated displacement field showing the circular standing flexural waves in the glass slide in the 2D axisymmetric model with an excitation of 109.2 kHz and 6 V_{pp}. **(b)** Simulated wave displacement amplitudes along the radial direction under different driving voltages. **(c)** Simulated acoustic pressure amplitude distribution in the droplet. **(d)** Simulated acoustic streaming field in the droplet. **(e)** Simulated distributions of tangential acoustic streaming velocity at the outside boundary of the viscous boundary layer for $0 < r < 1.3$ mm under different driving voltages. **(f)** Relationship between u_{max}, u_{mean}, and driving voltage. **(g)** Simulated distributions of tangential acoustic streaming velocity at the outside boundary of the viscous boundary layer for $0 < r < 1.3$ mm under different droplet volumes. **(h)** Relationship between u_{max}, u_{mean}, and droplet volume.

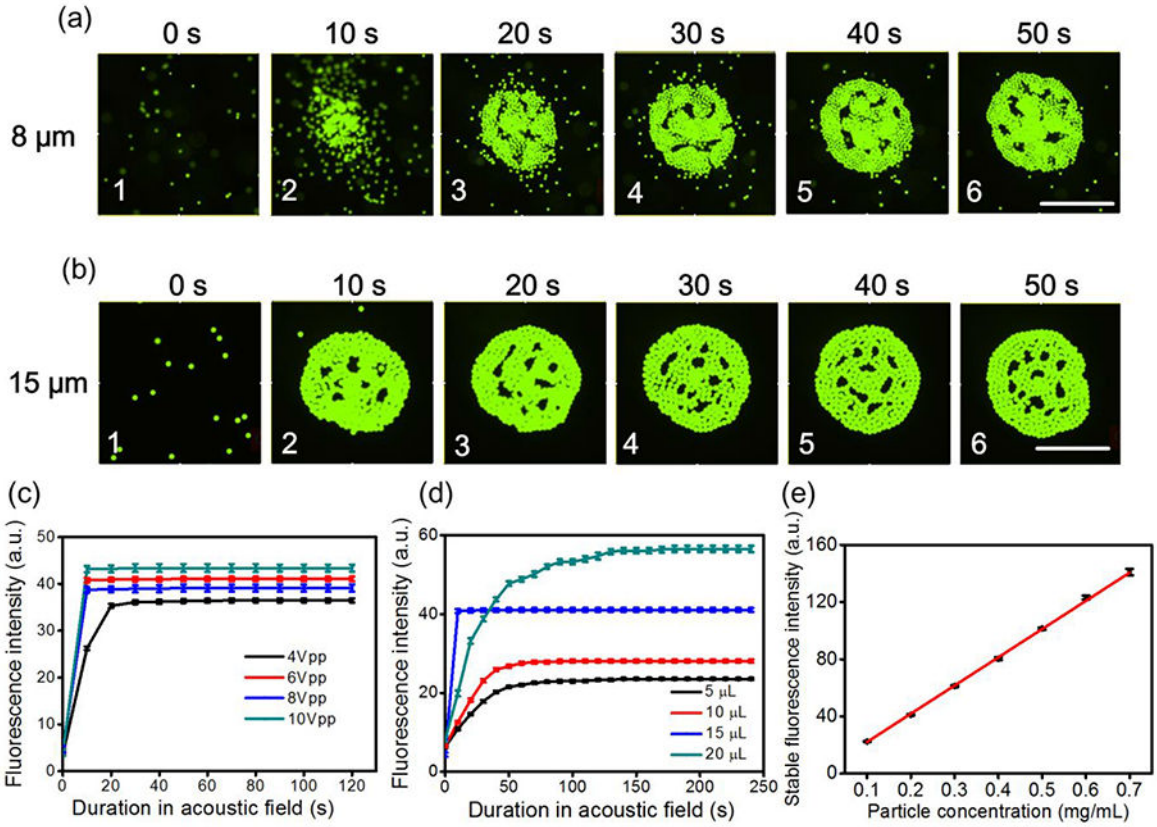

Figure 3.

(a) Concentration process of 8 μm fluorescent polystyrene particles within a single unit of the acoustofluidic multi-well plate when the driving voltage, frequency, droplet volume, and particle concentration are 6 V_{pp}, 112 kHz, 15 μL, and 0.10 mg/mL, respectively. Scale bar: 500 μm. **(b)** Concentration process of 15 μm fluorescent polystyrene particles within a single unit of the acoustofluidic multi-well plate when the driving voltage, frequency, droplet volume, and particle concentration are 6 V_{pp}, 112kHz, 15 μL, and 0.20 mg/mL, respectively. Scale bar: 500 μm. **(c)** Fluorescence intensity versus acoustic field time under different driving voltages for 15 μm fluorescent polystyrene particles when the droplet volume and particle concentration are 15 μL and 0.20 mg/mL, respectively, **(d)** Fluorescence intensity versus acoustic field time under different droplet volumes for 15 μm fluorescent polystyrene particles when the driving voltage and particle concentration are 6 V_{pp} and 0.20 mg/mL, respectively, **(e)** Relationship between the stable fluorescence intensity after acoustic field and particle concentration for 15 μm fluorescent polystyrene particles when the diving voltage and droplet volume are maintained at 6 V_{pp} and 15 μL, respectively.

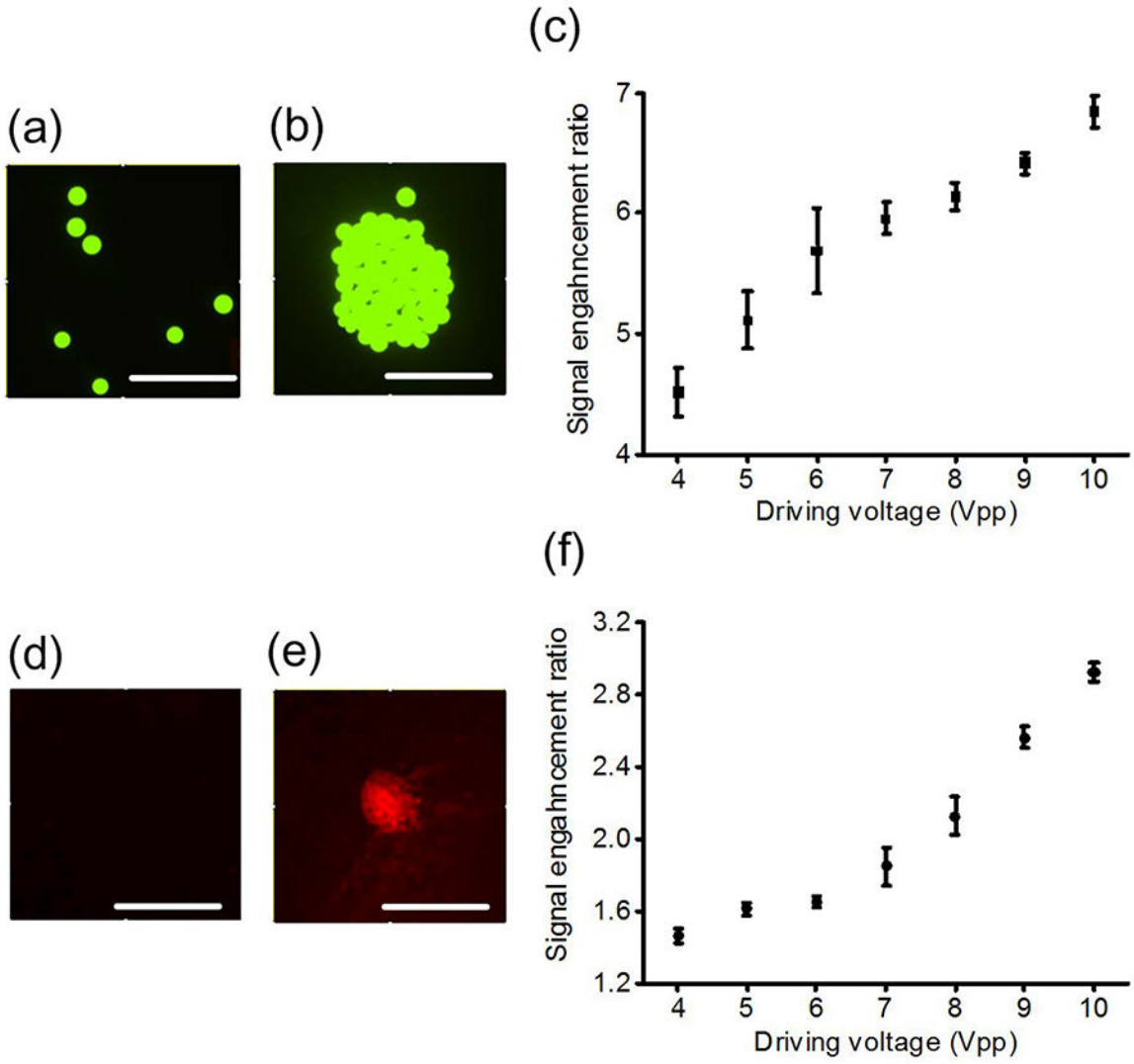

Figure 4.

(a) Initial random distribution of 30 μm polystyrene particles in the central area at the droplet-substrate interface when the droplet volume and particle concentration are 15 μL and 0.20 mg/mL, respectively, **(b)** Aggregation of 30 μm polystyrene particles after 10 s of acoustic field with a 6 V_{pp} driving voltage and 112 kHz excitation frequency, **(c)** Fluorescent signal enhancement ratio versus driving voltage for 30 μm polystyrene particles, **(d)** Initial random distribution of 470 nm carboxyl magnetic particles in the central area at the droplet-substrate interface when the droplet volume and particle concentration are 15 μL and 0.10 mg/mL, respectively, **(e)** Aggregation of 470 nm carboxyl magnetic particles after 1 min of acoustic field with an 8 V_{pp} driving voltage and 112 kHz excitation frequency, **(f)** Fluorescent signal enhancement ratio versus driving voltage for 470 nm carboxyl magnetic particles. Scale bars: 500 μm.

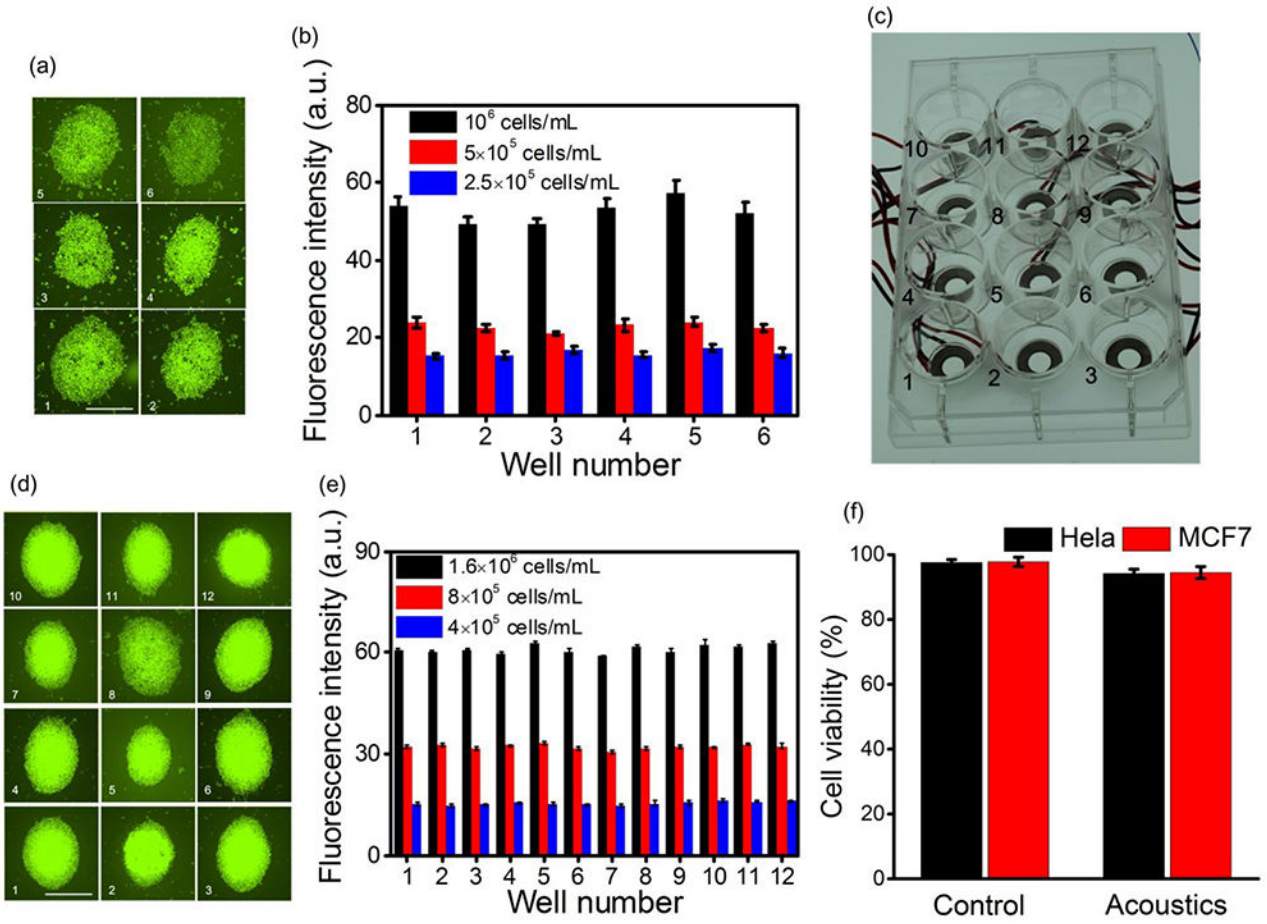

Figure 5.

(a) Stained MCF7 cell aggregations in wells 1-6 after 2 min of acoustic field when the driving voltage, frequency, droplet volume, and cell concentration are 10 V_{pp}, 110 kHz, 10 μL, and 10^6 cells/mL, respectively. Scale bar: 500 μm. **(b)** Fluorescence intensities of stained MCF7 cell aggregations in wells 1-6 after 2 min of acoustic field under different cell concentrations, **(c)** Photograph of the fabricated acoustofluidic 12-well plate, **(d)** Stained Hela cell aggregations in wells 1-12 after 2 min of acoustic field when the driving voltage, frequency, droplet volume, and cell concentration are 10 V_{pp}, 109 kHz, 10 μL, and 1.6×10^6 cells/mL, respectively. Scale bar: 500 μm. **(e)** Fluorescence intensities of stained Hela cell aggregations in wells 1-12 after 2 min of acoustic field under different cell concentrations. **(f)** Measured cell viabilities for MCF7 and Hela cells in a single well of the acoustofluidic multi-well plate under two conditions: without acoustic field (control) and with acoustic field.